



# Attitude Determination for Small Satellites with Infrared Earth Horizon Sensors

Tam Nguyen\* and Kerri Cahoy†

Massachusetts Institute of Technology, Cambridge, Massachusetts 02139  
and

Anne Mariman‡

California Institute of Technology, Pasadena, California 91109

DOI: 10.2514/1.A34010

Infrared Earth horizon sensors are capable of providing attitude knowledge for satellites in low Earth orbit by using thermopile measurements of the Earth's infrared emission to locate the Earth's horizon. Because some small satellites, such as CubeSats, have limited resources, a framework was developed that improves the attitude determination performance of an Earth horizon sensing system consisting of inexpensive thermopiles in static dual-mount configurations by leveraging mission geometry properties and improving sensor models. This paper presents an analytical approach to generate an estimate of the nadir vector in the satellite's body frame from Earth horizon sensor measurements. On-orbit telemetry data from the Microsized Microwave Atmospheric Satellite (MicroMAS) during limb-crossing events were used to assess our model of sensor readings in response to Earth horizon detection. To quantify the expected attitude estimation performance of our method, a detailed simulation of a low-Earth-orbiting satellite was developed with Earth horizon sensors in similar configurations to the MicroMAS sensor system. Our attitude determination method returns an error of  $0.16^\circ$  on average (root-mean-square error of  $0.18^\circ$ ) in nadir estimation under a periodic low-frequency attitude disturbance of  $4^\circ$ . A sensitivity analysis was conducted, which takes mounting uncertainty and position error into account, resulting in an additional attitude error of  $0.3^\circ$  for a mounting offset of  $0.2^\circ$  and up to  $0.13^\circ$  error for a 10-km position knowledge error.

## Nomenclature

$a$	=	Earth's equatorial radius
$f$	=	Earth's flattening factor
$\hat{p}, \hat{p}'$	=	two possible nadir unit vector solutions
$R$	=	sensor responsivity function
$r$	=	spacecraft position vector
$S$	=	area of sensor's field-of-view obstructed by Earth
$S_{\text{eff}}$	=	effective sensor reading
$\hat{S}_1, \hat{S}_2$	=	sensors' boresight unit vectors
$\alpha$	=	angular distance between sensor boresight and nadir vector
$\epsilon$	=	sensor's half-angle field of view
$\rho$	=	angular radius of Earth looking from spacecraft
$\theta_{\text{gc}}$	=	geocentric latitude of spacecraft
$\phi_1, \phi_2$	=	angle between nadir vector and sensors' boresight vectors

high-accuracy attitude knowledge [5], they are typically expensive and may exceed volume and power constraints for resource-limited small satellites such as CubeSats. Recent development has demonstrated that two-axis Sun sensors can achieve an attitude knowledge of better than  $0.5^\circ$  [6]. Disadvantages of Sun sensors come from their loss of functionality during eclipse periods. Because the Earth is large and bright in the infrared during both sunlight and eclipse for satellites in low Earth orbit (LEO), sensors that can detect the Earth's limb in the infrared can be used by the ADCS system to provide nearly uninterrupted fine attitude knowledge [7]. Infrared Earth horizon sensors have recently been implemented for CubeSat attitude determination in the format of a nine-sensor module, achieving a nadir estimation of  $0.5^\circ$  along two axes [6]. In this work, we present a new approach in nadir sensing, using only two infrared Earth sensors, along with four additional reference sensors, to accomplish a  $1\sigma$  nadir estimation error of less than  $0.2^\circ$ .

Infrared Earth horizon sensors (EHS) are effective and relatively inexpensive means of attitude determination for small satellites in LEO and are well-suited for Earth-observing missions [8]. Infrared EHS systems detect the Earth's electromagnetic radiation from solar radiation being absorbed and re-radiated by the Earth's surface and atmosphere. In the long-wave infrared spectrum, the Earth becomes a dominant infrared radiation source [9]. Infrared Earth horizon sensors have been used in large Earth-orbiting spacecraft, often achieving attitude knowledge accuracy of within  $5^\circ$  [7,8,10]. Thermal detectors, such as thermopiles, are commonly used for horizon detection. The thermopile detectors, often consisting of thermocouples in series or in parallel, generate an electrical output signal that is proportional to the amount of thermal energy detected [11]. Many thermopile-based horizon sensing systems include optics to reduce the effective field of view (FOV), lowering the probability of interference by the Sun and Moon [12]. The signal generated by the detector as its FOV sweeps across the Earth's horizon is a function of the horizon's magnitude and shape as seen in the FOV and distorted by the sensor's responsivity [10]. While EHS systems on large spacecraft often include moving parts for horizon scanning [10], it is more practical for small satellites to have fixed, body-mounted EHS systems due to mass, volume, and power limitations. The mission orbit and altitude along with the sensors' FOV and the mission objectives affect where the thermopiles are mounted on the satellite.

## I. Introduction

ATTITUDE determination and control systems (ADCS) are necessary for satellites on orbit to counter disturbances in nominal operation and to achieve mission requirements. Satellites typically use multiple sensors, such as Sun sensors, magnetometers, and star trackers for attitude determination [1–4]. Magnetometers are often used for coarse attitude determination due to the variability of the Earth's magnetic field. While star trackers are capable of providing

Presented at the 28th Annual AIAA/USU Conference on Small Satellites, Logan, UT, 4–8 August 2014; received 16 June 2017; revision received 28 March 2018; accepted for publication 20 April 2018; published online Open Access 30 July 2018. Copyright © 2018 by the American Institute of Aeronautics and Astronautics, Inc. All rights reserved. All requests for copying and permission to reprint should be submitted to CCC at [www.copyright.com](http://www.copyright.com); employ the ISSN 0022-4650 (print) or 1533-6794 (online) to initiate your request. See also AIAA Rights and Permissions [www.aiaa.org/randp](http://www.aiaa.org/randp).

\*Graduate Student, Department of Aeronautics and Astronautics, 77 Massachusetts Avenue 37-346.

†Associate Professor, Department of Aeronautics and Astronautics, 77 Massachusetts Avenue 37-367.

‡Systems Engineer, Jet Propulsion Laboratory, 4800 Oak Grove Dr. M/S 301-170S.

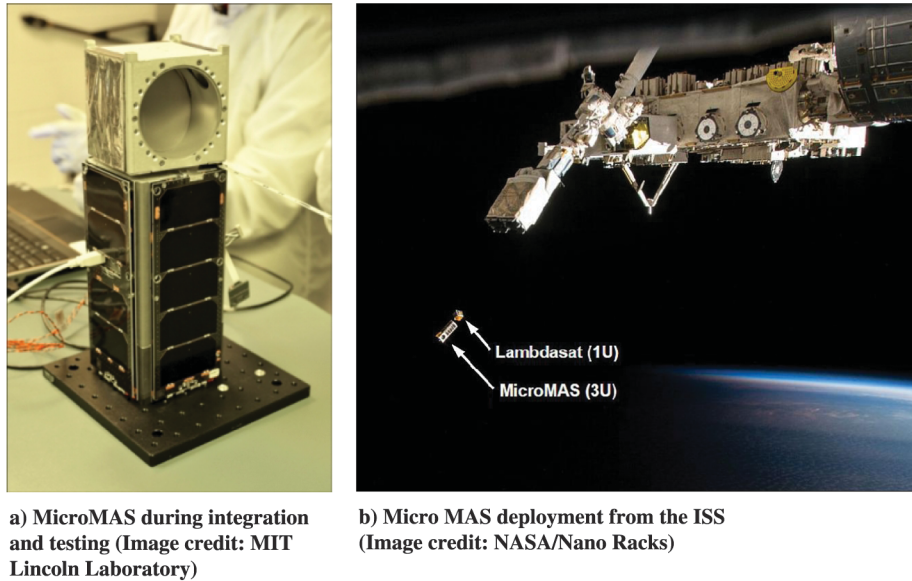


Fig. 1 MicroMAS during a) integration and testing and b) deployment.

Arrays of thermopiles have been used by small satellites to maintain nadir-pointing by radiance balance techniques, ensuring zero temperature difference between sensors in each sensor pair in opposite directions [6].

A recently developed static infrared EHS system was implemented on the Microsized Microwave Atmospheric Satellite (MicroMAS), a CubeSat mission developed jointly by the Massachusetts Institute of Technology (MIT) and MIT Lincoln Laboratory [13]. This EHS system consists of only two static sensor mounts, each with a total of four miniaturized thermopile sensors (including reference sensors), offering a significant reduction in mass and volume compared with previous existing EHS systems. While previous work in literature has offered valuable insights on the use of individual infrared sensors and arrays of thermopiles for horizon sensing, no previous work has been done in formulating a high-accuracy attitude determination method using a dual, static EHS system, like the one used by MicroMAS. The knowledge gap remains on how to effectively convert thermopile sensor readings from two static sensor assemblies into a single reference vector to be used in attitude determination.

MicroMAS, sometimes referred to as MicroMAS-1 is a 3U CubeSat (approximately 10 cm  $\times$  10 cm  $\times$  34 cm) with a spinning 1U passive microwave radiometer as the primary payload and a three-axis stabilized 2U bus [13,14]. The fully assembled satellite is shown in Fig. 1a. The goal of MicroMAS is to demonstrate weather observations on a small and low-cost satellite platform [13]. The MicroMAS ADCS consists of magnetometers, coarse Sun sensors, and Earth horizon sensors for attitude determination, and a set of three reaction wheels and three magnetorquers for attitude control [14,15]. The bus pointing requirement is  $1^\circ$  ( $3\sigma$ ) as derived from high-level mission requirements [14]. MicroMAS was launched on July 13, 2014, and deployed from the International Space Station (ISS) on March 4, 2015, as shown in Fig. 1b. Because of a communications failure 2 weeks into the mission, MicroMAS was unable to operate the payload and collect scientific data [16,17]. While no three-axis stabilized sensor data was collected, a 3-min long stream of telemetry data from the attitude sensors was downlinked on March 5, 2015, while the satellite was tumbling. The Earth horizon sensor data during this period was used to evaluate the sensors' functionality on orbit and assess our model of sensor response during horizon detection.

In this work, we focus on the performance analysis of the EHS system as used in the MicroMAS mission. The MicroMAS EHS system was part of the MAI-400 unit, an ADCS module from Maryland Aerospace, Inc. [18,19]. The coordinate system of MicroMAS is defined as follows: the  $+x$  direction is along the nominal velocity vector, the  $+z$  direction nominally points toward

nadir, and the  $+y$  direction points to the side of the spacecraft, completing a right-hand coordinate system, as shown in Fig. 2a. The EHS system consists of two orthogonally mounted sensor assemblies: one in the  $-x$  (antiram) direction and one in the  $+y$  (side) direction. Each mount consists of 4 EHS: one coarse sensor with approximately  $60^\circ$  FOV and 3 fine sensors with FOV of approximately  $10^\circ$  each.<sup>§</sup> The three fine sensors' boresights have distinct dip angles and are used as Earth, horizon (limb), and space sensors during nominal operation. This technique is used to overcome the Earth's complex thermal variations due to seasonal and weather factors. The coarse EHS are used to provide rough attitude knowledge, bringing the fine EHS sensors into the desired Earth, limb, and space configuration. The sensor values from the Earth and space EHS are used as the "hot" and "cold" references to normalize the limb sensor reading for fine attitude sensing capability. The use of a narrower FOV for the fine sensors also reduces the effect of solar interference. From orbit geometry analysis, the side-facing fine horizon sensor is not affected by solar interference in nominal operation configuration. Solar interference is still expected to occur on the antiram fine sensors approximately every 30 days, which will last for less than 5 min per orbit for consecutive orbits within a 3- to 4-day period. For these periods, attitude information from the antiram sensors will be limited; the system will rely on other attitude sensors to maintain relative pointing until the antiram sensors return to operational mode. Figures 2a–2c illustrate the MicroMAS EHS coarse and fine boresight and FOV configurations. The hardware for the MicroMAS  $+y$  assembly is shown in Fig. 2d.

We present an analytical approach to computing a nadir vector estimation from two horizon sensor readings using orbit geometry and sensor system configuration. This approach was developed to be compatible with limited processing and memory resources on small satellites. We used MicroMAS on-orbit telemetry data during limb-crossing events to evaluate our predicted sensor response during Earth horizon detection. To quantitatively assess the system's fine pointing capability, we created a detailed simulation of a LEO small satellite in AGI Systems Tool Kit (STK) and MATLAB with fine horizon sensor configuration similar to that of MicroMAS as shown in Figs. 2a–2c. The simulation results show the angular error between the nadir vector estimate computed from the simulated horizon sensor data and the "truth" nadir direction. We conducted sensitivity analyses to assess the attitude knowledge accuracy sensitivity to mounting error and position uncertainty.

<sup>§</sup>The sensors' FOVs were defined as the full-width at half-max (FWHM) of the sensors response curves.

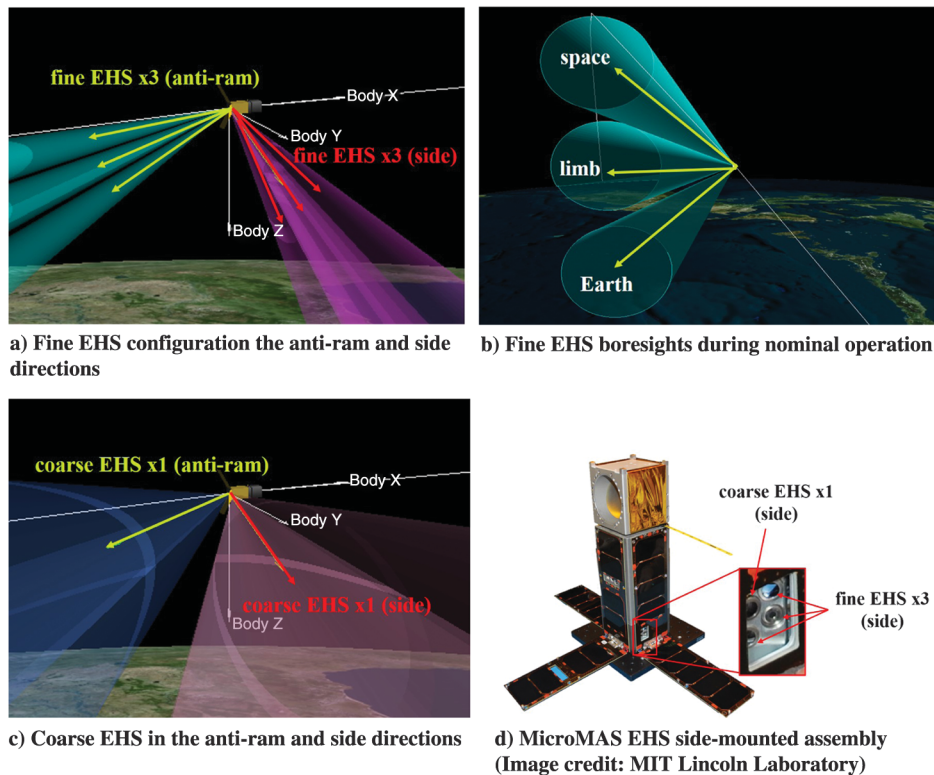


**Fig. 2** MicroMAS Earth-horizon sensing system configuration. Figures 2a–2c are generated using the Analytical Graphics, Inc. (AGI), Systems Tool Kit (STK) software with MicroMAS orbit and sensors configuration.

## II. Attitude Determination

### A. Method Overview

The attitude determination technique described in this paper consists of two main steps: nadir angle estimation and nadir vector estimation. The first step focuses on the conversion of the horizon sensor measurement to the corresponding angle between the sensor boresight and the nadir vector through a baseline model of the Earth and sensor geometry. To reduce complexity, the sensor to nadir angle method relies on the following assumptions: 1) the Earth infrared emission at the wavelength of interest is uniform within the sensor's FOV, and 2) the horizon observed by the sensor is sharp and circular. The first assumption can be applied to narrow FOV horizon sensors with a small footprint on the Earth's surface.<sup>†</sup> The second assumption can be applied when the Earth's infrared horizon distortion due to the atmosphere is insignificant compared with other noise sources, such as the uncertainty in the radius of the Earth due to ephemeris error, which will be further discussed in Sec. V.B. The effects of atmospheric and seasonal phenomena on the Earth horizon shape can be mitigated by the use of band-pass filters in the long-wave infrared range, specifically in the 14–16  $\mu\text{m}$  band, where filters are also commercially available [20]. The sensor reading can be assumed to be proportional to the area obstructed by Earth in the sensor's FOV. The nadir vector estimation provides an analytical solution of the nadir unit vector given two nadir angles as measured from horizon sensors with independent boresight vectors. In Secs. II.B and II.C, we provide detailed descriptions of the nadir angle estimation and nadir vector estimation, respectively.

### B. Nadir Angle Estimation

The sensor reading is a function of the area obstructed by Earth in the sensor's FOV, which is modeled as the overlap area between the projections of the sensor's FOV and the Earth onto the spacecraft-centered unit sphere. Both projections are modeled as circles with known angular radii. The center of the sensor field projection on the

spacecraft-centered sphere represents the direction of the sensor boresight, and the center of the Earth disk denotes the direction of the nadir vector. A graphical representation of the projection geometry is shown in Fig. 3.

The overlap area  $S$  between the projections of the sensor's FOV of radius  $\epsilon$  and the Earth disk of radius  $\rho$  represents the region obstructed by Earth within the sensor's FOV. The angle between the nadir vector and the sensor boresight is denoted by  $\alpha$ . When  $\alpha \geq \rho + \epsilon$ , the two circular projections do not overlap, representing the case where Earth is not detected by the sensor. When  $\alpha \leq \rho - \epsilon$ , the sensor's FOV is fully obstructed by Earth, assuming that the sensor's FOV is narrower than the Earth disk. The Earth's horizon is detected by the sensor when  $\alpha$  is within the range  $(\rho - \epsilon, \rho + \epsilon)$ . The overlap area  $S$  in this range can be computed mathematically as a function of  $\alpha$ ,  $\epsilon$ , and  $\rho$  as shown in Eq. (1) [8]. For known values of  $\epsilon$  and  $\rho$ , this relationship allows the sensor reading, which can be directly correlated to  $S$ , to be converted to a nadir angle relative to a fixed and known vector in the spacecraft body frame, leading to partial attitude knowledge. Because it is computationally intensive to invert this equation to solve

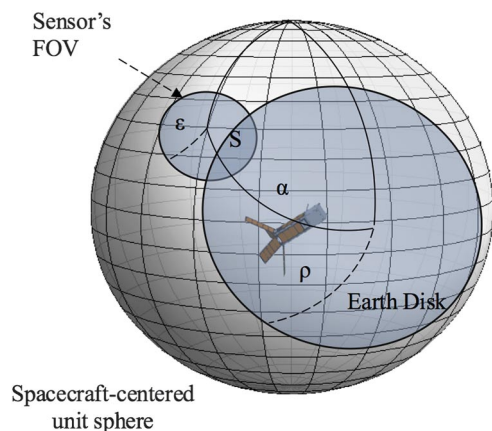


**Fig. 3** Projections of the sensor's FOV and Earth on the spacecraft-centered unit sphere.

<sup>†</sup>MicroMAS's fine sensors have roughly 50 km footprint in diameter from the intended orbit (approximately 400 km in altitude).

for  $\alpha$  as a function of  $S$ , creating a look-up table is more practical for software implementation of this method.

$$S(\alpha, \epsilon, \rho) = 2 \left( \pi - \cos(\rho) \cos^{-1} \left( \frac{\cos(\epsilon) - \cos(\rho) \cos(\alpha)}{\sin(\rho) \sin(\alpha)} \right) - \cos(\epsilon) \cos^{-1} \left( \frac{\cos(\rho) - \cos(\epsilon) \cos(\alpha)}{\sin(\epsilon) \sin(\alpha)} \right) - \cos^{-1} \left( \frac{\cos(\alpha) - \cos(\epsilon) \cos(\rho)}{\sin(\epsilon) \sin(\rho)} \right) \right) \quad (1)$$

Because the sensor’s response curve, often provided by the manufacturer, does not follow a uniform “top-hat” profile with clear cut-off at the specified FOV, we compute the effective sensor reading as a function of the overlap function presented in Eq. (1) and the sensor response curve  $R(e)$ , where  $e$  represents the off-boresight angle. The effective sensor reading can be modeled as the overlap area between the Earth disk and the sensor’s FOV, modified by the sensor’s response curve. Conceptually, the effective sensor reading calculation can be described as the weighted sum of multiple overlap regions of constant responsivity, where the weight can be distributed following the sensor’s response curve from the manufacturer. Figure 4 illustrates this concept with three regions, computed using Eq. (1) with different sensor angular radii parameter  $e$  to the corresponding FOV half-angle of each sensor region. The sensor response becomes the weighted sum of the overlap regions with the appropriate coefficients as derived from the sensor’s response curve. Equation (2) presents the general analytical form of the effective sensor reading for given values of nadir angle  $\alpha$  and Earth disk radius  $\rho$ , with infinitesimal sensor region size ( $de$ ), sensor response function  $R$ , and overlap function  $S$ . The equation can be written in integral form as shown in Eqs. (3) and (4). Figure 5 shows the sensor response

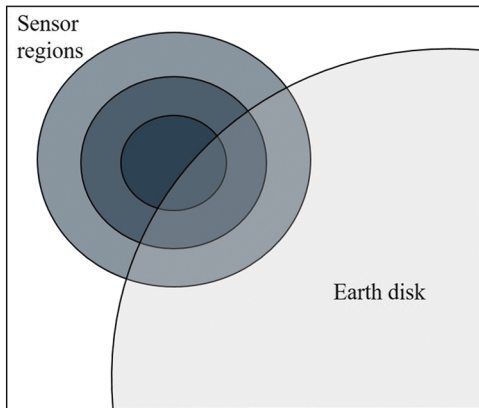


Fig. 4 Obscuration model with sensor field divided into regions of constant sensitivity.

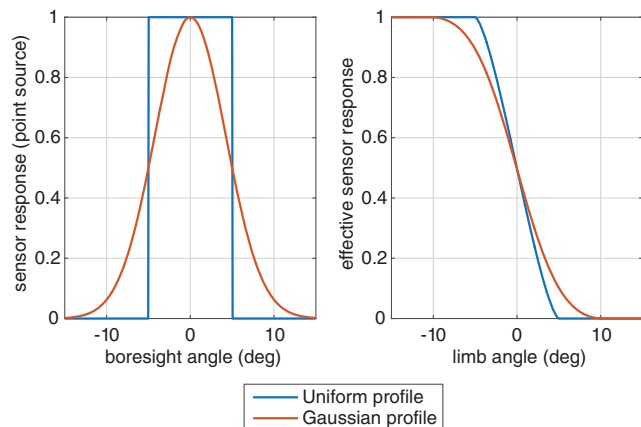


Fig. 5 Sensor response (left) and effective horizon sensor reading (right) with uniform and Gaussian sensor responsivity profiles.

curve and corresponding horizon sensor reading as a function of horizon off-boresight angle. The “uniform” profile in blue represents a “top-hat” sensor response curve where  $R$  is constant within the arbitrarily specified FOV ( $10^\circ$  full angle). In this extreme case, the corresponding horizon sensor reading is the same as the overlap area function  $S$ . In reality, most sensors do not have uniform responsivity but often have a more Gaussian shape, as shown in Fig. 5 in red, where the FOV is defined as the FWHM of the Gaussian curve. The sensor response shown in red in Fig. 5 (right) shows a realistic response for a Gaussian-shaped sensor responsivity as the sensor sweeps across the Earth’s horizon. The sensor response values can be precomputed for different values of nadir angles to construct a look-up table. This look-up table, consisting of the modified sensor response and the corresponding nadir angle, can be saved in the system memory for efficient on-orbit nadir angle conversion.

$$S_{\text{eff}}(\alpha, \rho) = \lim_{\Delta e \rightarrow 0} \sum_{e=0}^{\infty} R(e) [S(\alpha, e + \Delta e, \rho) - S(\alpha, e, \rho)] \quad (2)$$

$$= \int_0^{\infty} R(e) \frac{\partial S(\alpha, e, \rho)}{\partial e} de \quad (3)$$

$$= R(e) S(\alpha, e, \rho) \Big|_{e=0}^{\infty} - \int_0^{\infty} R'(e) S(\alpha, e, \rho) de \quad (4)$$

We initially assumed that the half-angle subtended by Earth from the satellite’s reference frame, denoted by  $\rho$ , was constant in the previous analysis. However, this assumption results in significant attitude estimation inaccuracy in the case of satellites in high-eccentricity orbits or satellites that are de-orbiting. Because many LEO satellites have position knowledge through the Global Positioning System (GPS) or Two-line Element (TLE) data, this information can be used to dynamically estimate the angle subtended by Earth in the satellite’s frame  $\rho$ , improving the attitude estimation accuracy.

The half angle subtended by the Earth in the satellite’s reference frame,  $\rho$ , is a function of the orbit radius and the Earth radius at the horizon. For satellites with low altitude, the Earth radius can be approximated as the Earth radius at the subsatellite point. The Earth’s half-angle  $\rho$  can be approximated as shown in Eq. (5), where  $r$  represents the satellite’s position vector in an Earth-centered reference frame. The orbit radius is computed as the magnitude of the position vector. The Earth radius at the subsatellite point can be computed using the standard World Geodetic System 84 Ellipsoid Earth model, where  $a$  is the equatorial Earth radius,  $f$  is the flattening factor, and  $\theta_{gc}$  is the geocentric latitude of the satellite [21].

$$\rho(r) \approx \sin^{-1} \left( \frac{a(1 - f \sin^2 \theta_{gc})}{|r|} \right) \quad (5)$$

A change in  $\rho$  induces a shift in the EHS response curve, as shown in Fig. 6, where the limb angle is defined as the difference between the nadir angle and the nominal Earth disk angular size  $\rho_0$ . To avoid recalculating the horizon sensor’s response  $S_{\text{eff}}$  with changing  $\rho$  value, one EHS look-up table for a nominal value of  $\rho$  can be saved in system’s memory and a correction term can be calculated to accommodate variations in  $\rho$ . In most cases, only a shift term is needed, equal to the amount of Earth’s disk size variation  $\Delta\rho$  because the curve distortion is relatively small. For instance, the accuracy of this sensor response approximation is better than 0.1% for altitude variations of less than 100 km from a nominal ISS orbit. If better accuracy is desired for the mission, multiple look-up tables at representative altitudes can be pregenerated and interpolation can be used in flight software to compute the corresponding sensor response curve such that the required on-board memory can be reduced.

C. Nadir Vector Estimation

At least two nadir angles relative to distinct boresight vectors are needed to provide a finite set of nadir vector solutions. The problem

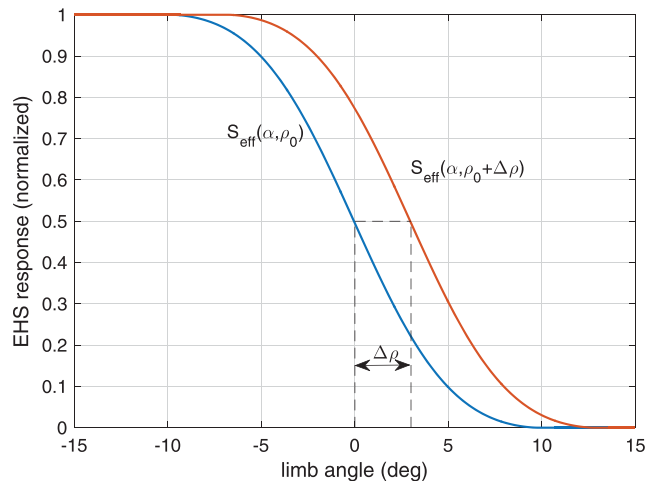


**Fig. 6** Response curve shift due to variation in Earth disk size  $\rho$  as the result of altitude variations.

becomes finding the intersection of two cones, each with a different axis direction, defined by the sensor boresight vector, and a cone angle, which is the nadir angle computed in Sec. II.B. The geometric solutions can be visualized using Fig. 7.  $\hat{S}_1$  and  $\hat{S}_2$  represent the sensor boresights;  $\phi_1$  and  $\phi_2$  are the corresponding nadir angles;  $\hat{P}$  and  $\hat{P}'$  are the intersections of the  $S_1$ -centered and  $S_2$ -centered cones, representing the two possible nadir vectors.

The analytical form of the possible nadir vectors is the solutions to the system of Eqs. (6). The first two equations ensure that the angles between the solutions and the boresight vectors are equal to the nadir angles found in Sec. II.B. The third equation in Eq. (6) is a normalization condition, which is required for the first two equations to hold. This system of three equations has three variables, which are the three components of the nadir vector. It can be solved analytically through variable elimination and substitution for a finite set of solutions. The analytical solutions in full-form are shown in the Appendix. Algebraically, there can be zero, one, or two vector solutions to the system of equations because the third equation is of second order. When both sensors detect the horizon, the system of equations has at least one solution, assuming relatively low sensor noise levels. The system of equations has exactly one solution when the satellite is oriented such that the nadir vector is on the plane containing  $\hat{S}_1$  and  $\hat{S}_2$ , which is unlikely to occur due to jitter and other disturbances. In most cases, there are two possible nadir vector solutions to the system of equations, leading to ambiguity in the estimation results.

$$\begin{aligned} \hat{P} \cdot \hat{S}_1 &= \cos(\phi_1) \\ \hat{P} \cdot \hat{S}_2 &= \cos(\phi_2) \\ |\hat{P}| &= 1 \end{aligned} \quad (6)$$

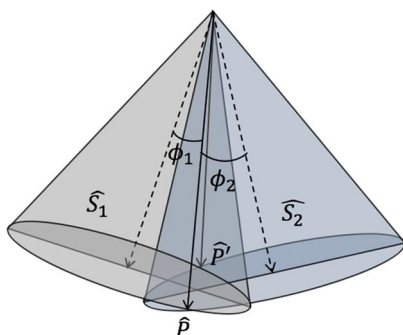


**Fig. 7** Graphical representation of the possible nadir vectors  $\hat{P}$  and  $\hat{P}'$ , with given two nadir angles  $\phi_1$  and  $\phi_2$  relative to two reference vectors  $\hat{S}_1$  and  $\hat{S}_2$ .

The physical interpretation of this ambiguity can be visualized in the scenarios presented in Fig. 8. The attitude shown in Fig. 8b is the result of rotating the satellite from the attitude in Fig. 8a about the boresight of one sensor until the other sensor detects the other side of the Earth's horizon. The two scenarios yield the same EHS readings because both sensors are obstructed by Earth by the same amount. However, in Fig. 8b scenario, the  $z$  axis of the spacecraft is no longer in alignment with the nadir vector as in Fig. 8a scenario.

The ambiguity can be resolved by the use of an additional coarse sensor, which is usually available within the satellite's ADCS. This sensor can be coarse given that the two possible EHS nadir vector solutions  $\hat{P}$  and  $\hat{P}'$  are well separated. It can be seen in the geometrical representation (Fig. 7) as well as proven algebraically that  $\hat{P}$  and  $\hat{P}'$  are reflections of each other through the plane containing vectors  $\hat{S}_1$  and  $\hat{S}_2$ . Therefore, the angle separation between  $\hat{P}$  and  $\hat{P}'$  is twice the angle between  $\hat{P}$  and the  $\hat{S}_1$ - $\hat{S}_2$  plane, as illustrated in Fig. 9. For a satellite in an ISS orbit like MicroMAS, the angle between the nadir vector and the nominal  $\hat{S}_1$ - $\hat{S}_2$  plane is approximately  $60^\circ$ .\*\* The angle separation between  $\hat{P}$  and  $\hat{P}'$ , denoted as  $\theta_{PP'}$ , can be computed as shown in Eq. (7).

$$\theta_{PP'} = 2 \left| \sin^{-1} \left( \hat{P} \cdot \frac{\hat{S}_1 \times \hat{S}_2}{|\hat{S}_1 \times \hat{S}_2|} \right) \right| \quad (7)$$

### III. On-Orbit EHS Telemetry from MicroMAS

On March 5, 2015, the Wallops ground station received telemetry from MicroMAS for 176 s from 2015-03-05 13:54:02 UTC to 13:56:58 UTC, while the spacecraft was tumbling. The data stream includes measurements from all eight infrared EHS and other attitude sensors such as the Sun sensors, IMU, and magnetometer. While the EHS in the antiram assembly (assembly B) show multiple Earth and Sun transits, the side assembly (assembly A) sensors consistently show a value of approximately 1450 counts, much higher than the expected Earth temperature. A thorough analysis of the blockage of this sensor by a solar panel failing to fully deploy is treated in Marinan et al. [16]. For this reason, only sensor data from assembly B were used to verify our sensor reading model in response to the Earth disk. The EHS readings from assembly B (antiram) are shown in Fig. 10. While this data set is not from a controlled attitude experiment but rather from postdeployment tumbling, the rising and falling edges of the Earth-crossing events allow us to evaluate the sensor reading model in response to the Earth disk as presented in Sec. II.B.

The data from EHS on assembly B show 3 Earth-crossing events, followed by partial to full solar glints. The occurrence of these events is consistent with results from other attitude sensors [16]. From an estimated attitude solution using a combination of sensor data, the EHS sensor ground track was moving from high latitudes toward the Equator at this time, which explains the gradual increase in the sensor measurement as it corresponds to an increase in the detected temperature of Earth along the sensor track.

The first set of rising edges from the fine sensors (at approximately  $t = 7$  to 10 s) was used to assess sensor and orbit models in Sec. II.B. These limb-crossing events are not contaminated by solar glints like the falling edges, and the spacecraft tumbling rate was slow enough to provide a reasonable number of sampled data points. Figure 11 shows the three rising edges, taken from three fine antiram EHS, overlaid with the expected limb-crossing curve as modeled in Sec. II.B, where the limb-crossing speed was inferred from gyro readings at this time.†† The measurements and model are scaled to a [0,1] range, where 0 indicates the value when the sensors are facing cold space and 1 indicates the values when the sensors are entirely obstructed by

\*\*The angle between the nadir vector and the nominal  $\hat{S}_1$ - $\hat{S}_2$  plane reduces with higher altitude due to steeper dip angles of the sensors. In the highest LEO altitude of 2000 km, this angle is approximately  $35^\circ$ .

††Note that the model input assumes an impact parameter of  $0^\circ$  and constant rotation over the span of the limb-crossing event (approximately 3 s).

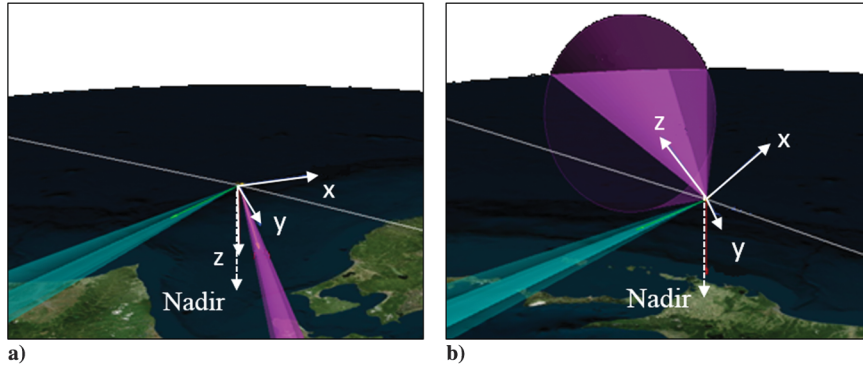


**Fig. 8** Ambiguity in attitude determination using EHS readings. The attitude in scenario (b) yields the same sensor readings as in scenario (a) while the satellite’s  $z$  axis is no longer in alignment with the nadir vector.

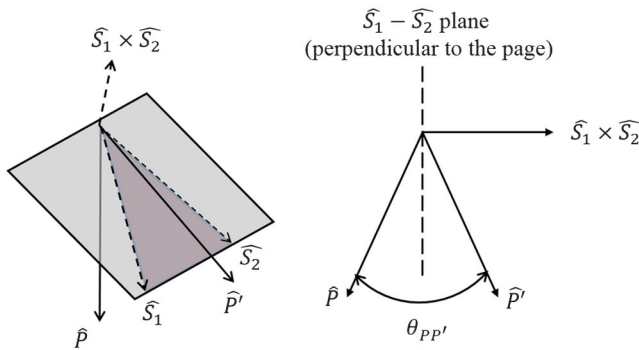


**Fig. 9** Geometric illustration of the angle separation between the two possible nadir vectors.

Earth. The root-mean-square (RMS) error between the flight data and model were calculated to be 0.021 (2.1% relative to Earth readings), showing agreement between the model presented in Sec. II.B and actual flight data from MicroMAS.

**IV. Attitude Determination Simulation**

**A. Simulation Description**

To assess the accuracy of the attitude estimation method presented above, a Systems Tool Kit (STK) model was created for a small satellite in LEO, deployed from the International Space Station (ISS) and propagated using the STK built-in High-Precision Orbit Propagator (HPOP) tool. The orbit profile used in this analysis is shown in Fig. 12. The altitude varies between 400 and 430 km within one orbit.

The sensor configuration is similar to the fine EHS configuration of MicroMAS with six sensors: three are mounted in the  $-x$  direction and three on the  $+y$  direction. All sensors have Gaussian sensitivity with FOV full angle of  $9.8^\circ$ . The three sensors on each assembly are arranged to look at deep space, the Earth’s horizon, and the Earth, and are tilted in the  $+z$  direction by  $7.3^\circ$ ,  $18.4^\circ$ , and  $30.0^\circ$ , respectively, as estimated from preflight MicroMAS boresight angle testing. The sensor looking at deep space is not obstructed by Earth and is used as a “cold” reference for the horizon sensor reading. Similarly, the sensor designated to look at Earth provides a “hot” reference for the horizon sensors. The obscuration percentage of the horizon sensor can be computed using these two references to mitigate the effect of varying infrared emission from Earth’s surface and background disturbances. In this simulation, the satellite is modeled to spin around the  $z$  axis, which initially aligns with the nadir vector. This spinning configuration is used to validate the performance of the EHS system with different portions of the Earth’s horizon being detected; it does not reflect the MicroMAS intended attitude. Attitude disturbances are manually introduced by setting a fixed nutation level for the spinning motion. In this analysis, the nutation level was set to be  $4^\circ$ , representing the extreme condition where the horizon can still be detected by the horizon sensors for the majority of the time during

the orbit. A graphical representation of the attitude setting is shown in Fig. 13. In addition, statistical noise level of the system, estimated from flight MicroMAS data, was applied to the simulated sensor readings before nadir vector estimation to improve the fidelity of the simulation.

**B. Simulation Results**

The estimated nadir vector can be compared with the nadir vector extracted directly from the STK model, which is considered to be the “truth” reference in this analysis. The STK obscuration tool was used to find the percentage of the sensor field obstructed by Earth. Given two horizon sensors, the attitude estimation method presented in Sec. II was used to compute a unique estimate of the nadir vector. Ambiguity is resolved by assuming that the satellite’s  $z$  axis is near nadir pointing. The nadir estimation method used in this simulation employs both sensor model adjustment for effective sensor readings and altitude correction using ephemeris data with a single look-up table, as described in Sec. II.B.

Figure 14 shows the nadir estimation error along the  $x$  and  $y$  axes of the body frame, computed by comparing the angular separation between the estimated nadir vector and the true nadir vector as defined in STK. The symmetry of this distribution suggests that there is no significant source of inherent bias in our method. We computed the absolute angular separation of the two vectors, equivalent to the mean distance of the distribution of  $x$  and  $y$  angles in spherical geometry. We found that the average angular separation between the estimated and true nadir vector is  $0.16^\circ$ . The RMS angular separation is  $0.18^\circ$ , which also represents the  $1\sigma$  deviation of the zero-mean  $x$  and  $y$  angular error distribution. The gaps in the data show the times when the horizon sensors have just missed the Earth horizon due to extreme disturbances. Figure 15 shows the errors in the  $x$ ,  $y$ , and  $z$  directions of the estimated nadir unit vector as compared with the true nadir unit vector over the duration of one orbit. The oscillatory behavior of the  $x$  and  $y$  components of the nadir vector is primarily caused by the “worst-case” nutation level of  $4^\circ$  injected into the simulation. It was observed that the nadir angle estimation from each boresight is more accurate when the Earth obscuration level is near 50% and degrades when this obscuration level deviates from the optimal level. The high-frequency noise is caused by statistical error, estimated from the MicroMAS on-orbit data stream and injected into the simulation in the sensor modeling module. In addition, it can be observed that the  $z$  component of the estimated nadir vector achieves higher accuracy than the  $x$  and  $y$  components, due to error propagation given the sensor system geometry.<sup>‡‡</sup>

Without taking into account the sensor sensitivity modeling and real-time altitude correction, the accuracy of the estimation is significantly reduced. When the sensor is modeled as having Gaussian characteristics, using the uniform sensitivity approxima-

<sup>‡‡</sup>The results presented here are prefiltering. Most ADCS implement Kalman filtering before computing a full attitude solution using multiple attitude sensors, which will significantly reduce the effect of statistical noise of the horizon sensors.

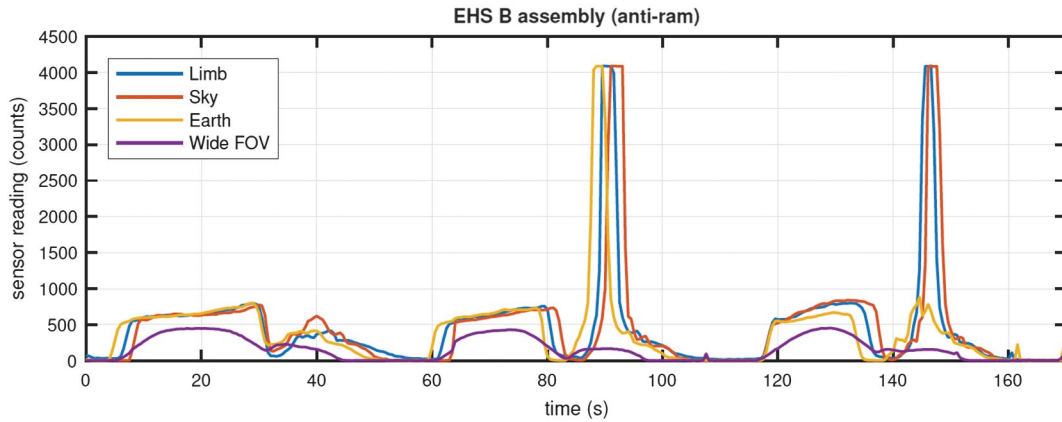


Fig. 10 MicroMAS telemetry data on March 5, 2015, for assembly B (antiram-mounted) EHS.

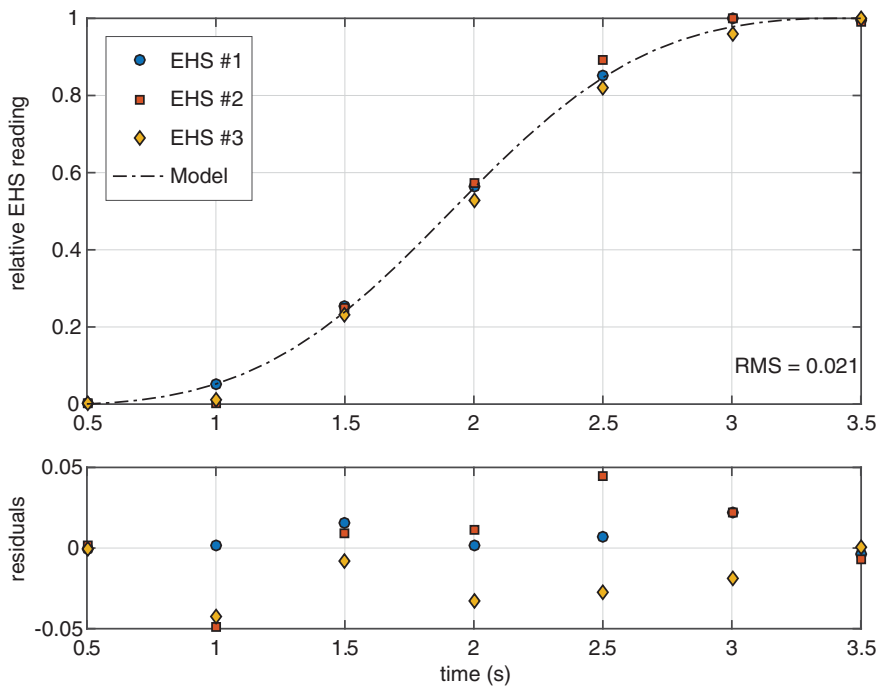


Fig. 11 EHS sensor readings from MicroMAS fine sensors during the first horizon-crossing event compared with modeled sensor response curve (RMS = 0.021).

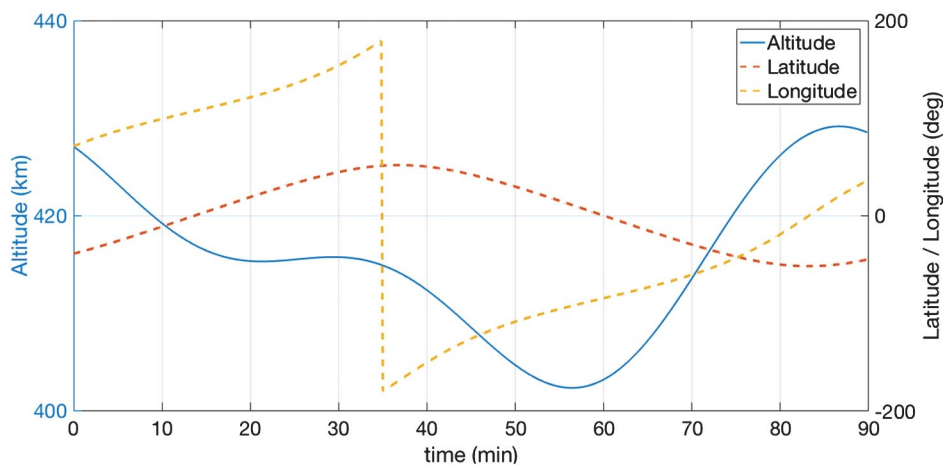


Fig. 12 Simulated orbit profile of a small satellite in LEO, deployed from the ISS.

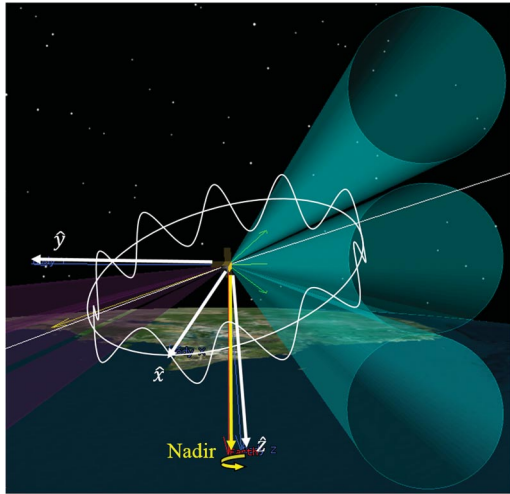


Fig. 13 Simulated attitude profile. The satellite rotates about nadir direction with a maximum disturbance level of  $4^\circ$ .

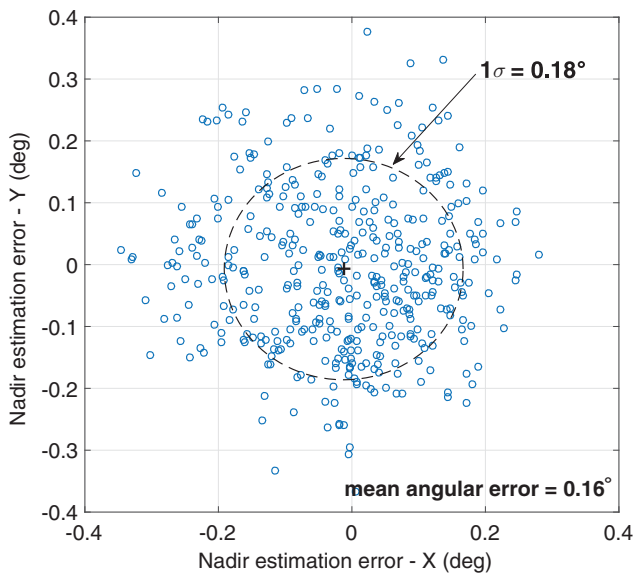


Fig. 14 Nadir estimation error in  $X$  and  $Y$ , representing the difference between the estimated nadir vector and the true nadir vector in STK, under a maximum disturbance level of  $4^\circ$ . The average angular error is  $0.16^\circ$ . The RMS error is  $0.18^\circ$ , which is equivalent to a  $1\sigma$  deviation for this distribution.

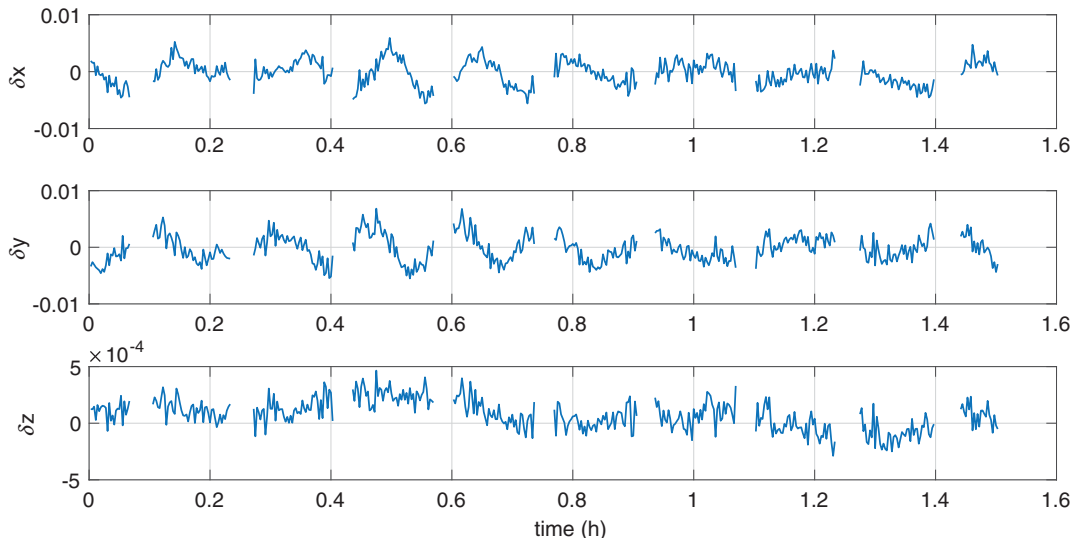


Fig. 15 The  $x$ ,  $y$ ,  $z$  components of the nadir vector error. The oscillatory behavior of the  $x$  and  $y$  components is caused by the “worst-case” nutation level injected into the simulation.

tion in the estimation process leads to an additional error of approximately  $0.95^\circ$ . If the satellite altitude is not corrected using position knowledge but assumed to be constant at an average value throughout the orbit, the attitude estimation error is increased by  $0.1^\circ$ . This error increase is expected to be higher for satellites in high-eccentricity orbits and in de-orbiting phase.

### V. Sensitivity Analysis

The simulation results in Sec. IV.B show the attitude knowledge accuracy of the horizon-sensing system with perfect knowledge of the sensors and orbit configuration. In reality, a number of system uncertainties could cause additional attitude knowledge error. In this section, we present the attitude knowledge error sensitivity to two major uncertainties: sensor mounting offset and satellite’s ephemeris (position) error.

#### A. Sensor Mounting Offset

The nadir estimation accuracy results presented in Sec. IV.B rely on perfect knowledge of the sensor boresight directions, which were used as body-fixed reference vectors. Because the sensor boresight directions do not align with the satellite’s body axes but are tilted in the  $z$  direction to allow horizon sensing, mounting errors are likely to occur during the assembly process of the sensor unit, mostly in the  $z$ -tilt angle. In addition, sensor mount directions are at risk of being displaced during the high-vibration launch environment. To assess the effect of mounting bias error on the performance of the system, different levels of boresight direction error were input to the model. The attitude accuracy performance results are shown in Fig. 16, where the blue data points indicate the results from boresight offset of one of the two assemblies and the red data points correspond to the case where both assemblies suffer from mounting error. The dashed lines show the corresponding best-fit second-order polynomial to the each of the data sets. It can be seen that the relationships between the boresight direction error and nadir estimation error in both cases follow a quadratic correlation. A mounting error of  $0.20^\circ$  on both assemblies leads to an additional error in nadir vector estimation of approximately  $0.30^\circ$  ( $0.17^\circ$  for error on a single assembly). Because of this high level of sensitivity, the attitude performance improves significantly when the sensor assembly boresight directions are accurately measured and unsusceptible to launch vibration.

#### B. Position Uncertainty

Because the nadir estimation relies on the satellite’s position to determine the Earth angular radius  $\rho$ , ephemeris uncertainty leads to additional error in attitude determination. Small satellites without GPS receivers rely on the North American Aerospace Defense

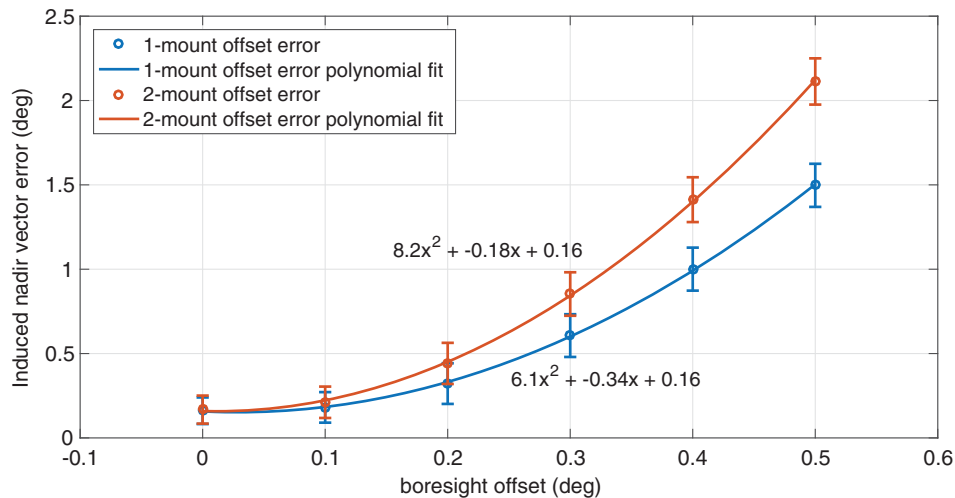


Fig. 16 Attitude error as a function of boresight offset of one or both of the EHS assemblies along with the corresponding polynomial fits.

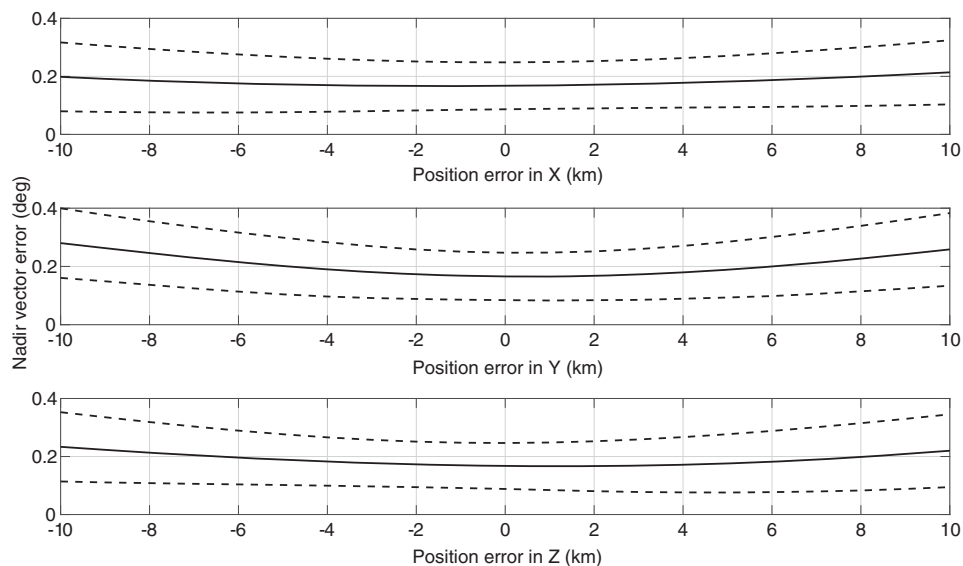


Fig. 17 Mean attitude error with  $1 - \sigma$  bounds as a function of satellite's position error.

Command (NORAD) Two-line Elements (TLEs) for position determination, which could result in position uncertainty of up to 10 km for ISS-deployed CubeSats [22]. To understand the effect of the satellite's position error on nadir estimation accuracy, position errors of up to  $\pm 10$  km are introduced to the simulation in each direction  $x$ ,  $y$ , and  $z$  in the Earth-centric Earth-fixed frame. The attitude accuracy results (mean and  $1\sigma$  standard deviation) are shown in Fig. 17. The average angular error of the nadir vector estimation increases by up to  $0.13^\circ$  with 10-km position error, doubling the baseline attitude error. The  $1\sigma$  standard deviation grows with position error, reaching up to  $0.12^\circ$  for 10 km position error. Small satellites in LEO equipped with Global Positioning System (GPS) receivers or other ranging devices can achieve better position knowledge, increasing the attitude accuracy of the Earth horizon sensing method.

## VI. Conclusions

This paper presents a method to provide satellite attitude knowledge by using two fixed body-mounted Earth horizon sensor assemblies. A nadir vector is computed in the satellite's body frame through extensive modeling of the orbit configuration and sensors' response. On-orbit data from the MicroMAS mission qualitatively confirm the sensor and orbit configuration models. The accuracy of the estimation method was verified through simulation to be  $0.16^\circ$  on average ( $0.18^\circ$  RMS), assuming that the sensors' responses, mounting directions, and position knowledge are known with high

precision. The estimation error increases quadratically with sensor boresight mounting error where a boresight offset of  $0.2^\circ$  on both assemblies leads to an additional error of  $0.3^\circ$ . The method's sensitivity to position error was also analyzed, showing that a position error of 10 km could lead to an additional nadir vector error of up to  $0.13^\circ$  on average.

While data from the MicroMAS mission were limited and insufficient to fully validate the method, this attitude determination technique has also been implemented on two satellites developed by MIT and MIT Lincoln Laboratory: 1) the Microwave Radiometer Technology Acceleration (MiRaTA) satellite, launched as a secondary payload with the Joint Polar Satellite System (JPSS-1), also known as the National Oceanic and Atmospheric Administration (NOAA-20), in November 2017 and 2) the MicroMAS-2 satellite, launched as a secondary payload on a Polar Satellite Launch Vehicle (PSLV-40) in January 2018. On-orbit controlled experiments will provide additional data to validate and improve the current attitude determination techniques with EHS systems.

## Appendix: Full-Form Analytical Solution of the Nadir Vector

Let  $\hat{P} = (P_x, P_y, P_z)$  be the nadir vector solution,  $\hat{S}_1 = (S_{1x}, S_{1y}, S_{1z})$  and  $\hat{S}_2 = (S_{2x}, S_{2y}, S_{2z})$  are the horizon sensor boresight vectors, and  $\phi_1$  and  $\phi_2$  be the nadir angle from  $S_1$  and  $S_2$ , respectively.

$P_z$  is the solution of the quadratic equation:

$$(A_x^2 + A_y^2 + 1)P_z^2 + 2(A_x B_x + A_y B_y)P_z + (B_x^2 + B_y^2 - 1) = 0$$

$$P_z = \frac{\sqrt{(A_x B_x + A_y B_y)^2 \pm 2(A_x^2 + A_y^2 + 1)(B_x^2 + B_y^2 - 1)}}{(A_x^2 + A_y^2 + 1)}$$

$$P_x = \frac{(\cos \phi_1 - S_{1z} P_z) S_{2y} - (\cos \phi_2 - S_{2z} P_z) S_{1y}}{S_{1x} S_{2y} - S_{1y} S_{2x}}$$

$$P_y = \frac{(\cos \phi_1 - S_{1z} P_z) S_{2x} - (\cos \phi_2 - S_{2z} P_z) S_{1x}}{S_{1y} S_{2x} - S_{1x} S_{2y}}$$

where

$$A_x = \frac{S_{2z} S_{1y} - S_{1z} S_{2y}}{S_{1x} S_{2y} - S_{1y} S_{2x}} \quad B_x = \frac{\cos \phi_1 S_{2y} - \cos \phi_2 S_{1y}}{S_{1x} S_{2y} - S_{1y} S_{2x}}$$

$$A_y = \frac{S_{1z} S_{2x} - S_{1x} S_{2z}}{S_{1x} S_{2y} - S_{1y} S_{2x}} \quad B_y = \frac{-\cos \phi_1 S_{2x} + \cos \phi_2 S_{1x}}{S_{1x} S_{2y} - S_{1y} S_{2x}}$$

### Acknowledgments

The authors would like to acknowledge the MicroMAS and MiRATA team at MIT and MIT Lincoln Laboratory as well as the Maryland Aerospace Inc. for their help and support in this work. We acknowledge support from the National Science Foundation Graduate Research Fellowship (NSF GRFP; Grant No. 1122374). This work was done as a private venture and not in the co-author's capacity as an employee of the Jet Propulsion Laboratory, California Institute of Technology.

### References

[1] Ortega, P., López-Rodríguez, G., Ricart, J., Domínguez, M., Castañer, L. M., Quero, J. M., Tarrida, C. L., García, J., Reina, M., Gras, A., et al., "A Miniaturized Two Axis Sun Sensor for Attitude Control of Nano-Satellites," *IEEE Sensors Journal*, Vol. 10, No. 10, 2010, pp. 1623–1632. doi:10.1109/JSEN.2010.2047104

[2] Theil, S., Appel, P., and Schleicher, A., "Low Cost, Good Accuracy—Attitude Determination Using Magnetometer and Simple Sun Sensor," *Proceedings of the 17th Annual AIAA/USU Conference on Small Satellites*, Paper SC03-XI-7, Logan, UT, 2003.

[3] Hales, J., and Pedersen, M., "Two-Axis MOEMS Sun Sensor for Pico Satellites," *Proceedings of the 16th Annual AIAA/USU Conference on Small Satellites*, AIAA/Utah State Univ., Logan, UT, 2002.

[4] Sarda, K., Grant, C., Chaumont, M., Choi, S. Y., Johnston-Lemke, B., and Zee, R., "On-Orbit Performance of the Bright Target Explorer (BRITE) Nanosatellite Astronomy Constellation," *Proceedings of the 28th Annual AIAA/USU Conference on Small Satellites*, Paper SSC14-XII-6, Logan, UT, 2014.

[5] Segert, T., Engelen, S., Buhl, M., and Monna, B., "Development of the Pico Star Tracker ST-200—Design Challenges and Road Ahead," *Proceedings of the 25th Annual AIAA/USU Conference on Small Satellites*, Paper SSC11-IX-4, Logan, UT, 2011.

[6] Janson, S., Hardy, B., Chin, A., Rumsey, D., Ehrlich, D., and Hinkley, D., "Attitude Control on the Pico Satellite Solar Cell Testbed-2,"

*Proceedings of the 26th Annual AIAA/USU Conference on Small Satellites*, Paper SSC12-II-1, Logan, UT, 2012.

[7] Astheimer, R., "High Precision Attitude Determination by Sensing the Earth and Lunar Horizon in the Infrared," *Automatica*, Vol. 7, No. 1, 1971, pp. 83–88. doi:10.1016/0005-1098(71)90082-3

[8] Wertz, J., *Spacecraft Attitude Determination and Control*, D. Reidel Publishing Company, Dordrecht, Holland, 1978, Chap. 7.

[9] Merrelli, A., "The Atmospheric Information Content of Earth's Far Infrared Spectrum," Ph.D. Thesis, Univ. of Wisconsin-Madison, Madison, WI, 2012.

[10] Thomas, J., and Wolfe, W., "NASA Space Vehicle Design Criteria (Guidance and Control): Spacecraft Earth Horizon Sensors," NASA Tech. Rept., 1969.

[11] Dehe, A., Fricke, K., and Hartnagel, H., "Infrared Thermopile Sensor Based on AlGaAs-GasAs Micromachining," *Sensors and Actuators A: Physical*, Vol. 47, Nos. 1–3, 1995, pp. 432–436.

[12] García Sáez, A., Quero, J. M., and Angulo Jerez, M., "Earth Sensor Based on Thermopile Detectors for Satellite Attitude Determination," *IEEE Sensors Journal*, Vol. 16, No. 8, April 2016, pp. 2260–2271.

[13] Blackwell, W., Allen, G., Galbraith, C., Leslie, R., Osaretin, I., Scarito, M., Shields, M., Thompson, E., Toher, D., Townzen, D., et al., "MicroMAS: A First Step Towards a Nanosatellite Constellation for Global Storm Observation," *Proceedings of the 27th Annual AIAA/USU Conference on Small Satellites*, Paper SSC13-XI-1, Logan, UT, 2013.

[14] Quadrimo, M. K., "Testing the Attitude Determination and Control of a CubeSat with Hardware-in-the-Loop," Master's Thesis, Massachusetts Inst. of Technology, Cambridge, MA, 2014.

[15] Wise, E., Pong, C., Miller, D., Nguyen, T., and Cahoy, K., "A Dual-Spinning, Three-Axis Stabilized CubeSat for Earth Observations," *Proceedings of the AIAA Guidance, Navigation, and Control (GNC) Conference*, AIAA Paper 2013-4716, 2013.

[16] Marinan, A., Hein, A., Lee, Z., Carlton, A., Cahoy, K., Milstein, A., Shields, M., DiLiberto, M., and Blackwell, W., "Analysis of the Microsized Microwave Atmospheric Satellite (MicroMAS) Communications Anomaly," *Journal of Small Satellites*, Vol. 7, No. 1, May 2018, pp. 683–699.

[17] Blackwell, W., and Pereira, J., "New Small Satellite Capabilities for Microwave Atmospheric Remote Sensing: The Earth Observing Nanosatellite-Microwave," *Proceedings of the 29th Annual AIAA/USU Conference on Small Satellites*, Logan, UT, 2015.

[18] "MAI-400 1/2U CubeSat ADACS," Maryland Aerospace, Inc., 2016, [http://maiaero.com/datasheets/MAI400\\_Specifications.pdf](http://maiaero.com/datasheets/MAI400_Specifications.pdf) [accessed May 2017].

[19] "MAI-SES Static Earth Sensor Product Specification," Maryland Aerospace Inc., 2016, <http://maiaero.com/datasheets/MAI-SES-Specifications-20150827.pdf> [accessed May 2017].

[20] Hanel, R., Bandeen, W. R., and Conrath, B. J., "The Infrared Horizon of the Planet Earth," *Journal of the Atmospheric Sciences*, Vol. 20, No. 2, 1963, pp. 73–86. doi:10.1175/1520-0469(1963)020<0073:TIHOTP>2.0.CO;2

[21] Macomber, M. M., "World Geodetic System 1984," Defense Mapping Agency, Washington, D.C., 1984.

[22] Riesing, K., "Orbit Determination from Two Line Element Sets of ISS-Deployed CubeSats," *Proceedings of the 29th Annual AIAA/USU Conference on Small Satellites*, Paper SSC15-VIII-5, Logan, UT, 2015.

J. McMahon  
Associate Editor